

Erbium and thulium on MgO(100)/Ag(100) as candidates for single atom qubitsS. Reale ^{1,2,3}, A. Singha ^{1,2,4}, S. L. Ahmed,^{1,5} D. Krylov,^{1,2} L. Colazzo,^{1,2} C. Wolf ^{1,2}, C. S. Casari ³, A. Barla ⁶, E. Fernandes,⁷ F. Patthey,⁷ M. Pivetta ⁷, S. Rusponi ⁷, H. Brune ⁷ and F. Donati ^{1,5,*}¹*Center for Quantum Nanoscience (QNS), Institute for Basic Science (IBS), Seoul 03760, Republic of Korea*²*Ewha Womans University, Seoul 03760, Republic of Korea*³*Department of Energy, Politecnico di Milano, Milano 20133, Italy*⁴*Max Planck Institute for Solid State Research, Stuttgart, Germany*⁵*Department of Physics, Ewha Womans University, Seoul 03760, Republic of Korea*⁶*Istituto di Struttura della Materia (ISM), Consiglio Nazionale delle Ricerche (CNR), I-34149 Trieste, Italy*⁷*Institute of Physics, Ecole Polytechnique Fédérale de Lausanne, 1015 Lausanne, Switzerland*

(Received 1 August 2022; accepted 30 November 2022; published 27 January 2023)

Lanthanide atoms on surfaces are an exceptional platform for atomic-scale magnetic information storage. However, their potential as qubits remains unexplored due to the limited number of experimental setups that can coherently drive the spins of single adatoms. Here we propose a combined experimental and theoretical method to estimate the performance of surface-adsorbed lanthanide atoms for quantum coherent operations. We investigate Er and Tm on MgO(100)/Ag(100) with x-ray absorption spectroscopy to address their magnetic and electronic properties and with scanning tunneling microscopy (STM) to identify their adsorption sites. With atomic multiplet calculations and density functional theory, we infer for both atoms a magnetic ground state that is suitable for quantum coherent operations. We investigate whether these systems lend themselves to electron spin resonance scanning tunneling microscopy (ESR-STM). By adapting the piezoelectric model of ESR-STM to the case of lanthanide atoms, we show that these systems should exhibit a detectable signal and that they have a higher Rabi rate compared to the systems studied up to date. In addition to their suitable electron spin properties, these elements possess a nontrivial nuclear spin that could be exploited to perform two-qubit operations on a single atom or to store quantum states in the nuclear spin.

DOI: [10.1103/PhysRevB.107.045427](https://doi.org/10.1103/PhysRevB.107.045427)**I. INTRODUCTION**

Atomic spin qubits on surfaces are novel, promising candidates in the burgeoning field of quantum coherent nanoscience [1]. The main advantages of these systems are their individual addressability with atomic-scale precision and the possibility to obtain ordered arrays or nanostructures exploiting atomic manipulation and self-assembly approaches [2–4]. Furthermore, the density of spins achievable with these systems [5] represents a significant advantage with respect to other qubit platforms for the future development of quantum control and sensing [1]. Up to now, the most promising way to address and control surface spin qubits has been to use electron spin resonance scanning tunneling microscopy (ESR-STM). This technique combines the spatial atomic resolution of STM with μeV energy resolution in continuous wave mode. In addition, in pulsed mode, ESR-STM allows the coherent spin manipulation of individual unpaired spins in atoms and molecules, which is necessary for their use as qubits [6–12].

The two most important requirements of a spin qubit are a long longitudinal relaxation time (T_1) and a long phase coherence time (T_2) [13]. The former is the time taken by the system to relax to the thermal equilibrium state. This process is characterized by a dissipation of energy to the environment taking

place by inelastic scattering with phonons or conduction electrons [14]. The latter, instead, characterizes the loss of phase relation between the spin and the control source due to elastic scattering. The coherence time is limited by the relaxation time through the relation $T_2 \leq 2T_1$, where the inequality accounts for additional decoherence sources in the environment and the perturbation of the drive. The central figure of merit of a qubit is the number of successive quantum operations that can be performed on it. It is also referred to as the qubit quality factor and is given by $Q = 2\Omega T_2$ [15], where Ω is the spin rotation rate (Rabi rate). Thus, a high Rabi rate and a long coherence time are necessary to have a good platform for quantum computation. For surface-adsorbed spin qubits investigated with ESR-STM, the Rabi rate is determined by the microwave power, tip, and tunneling conditions, which are typically optimized during the experiment. To achieve further improvement in the number of coherent operations, the usual approach is, therefore, to increase T_2 by decoupling the spin from the environment, effectively reducing the scattering with electrons and phonons from the substrate. For this reason, the spin-carrying atom is usually deposited on a decoupling layer [6,16–18] or embedded in a molecular structure [12]. However, STM requires a minimum conductance of the tunneling junction, which limits the thickness of the decoupling layer. Being a relatively new technique, only a limited number of spin qubit candidates, based on individual atoms [6,17,18], dimers [19], or molecules [12], have been studied using ESR-

*Corresponding author: donati.fabio@qns.science

STM. All these systems are characterized by a relatively short coherence time of the order of tens to hundreds of nanoseconds and Rabi rates up to tens of MHz, leading to a quality factor Q in the best cases of the order of unity [9,20]. However, present fault-tolerant quantum computation typically requires four to five orders of magnitude higher Q values [21].

An alternative way to isolate the spin from the environment is to localize it in well-shielded orbitals. This can be achieved with lanthanide atoms, which possess unpaired spins on the spatially localized $4f$ orbitals. The screening given by the other electrons occupying the external valence orbitals ($5s$, $5p$, $5d$, $6s$, and $6p$) provides some intrinsic decoupling of the spins from the environment. This phenomenon has been identified as the main contribution to the long T_1 [5,22–24] measured on individual surface adsorbed lanthanide atoms and T_2 measured on lanthanide atoms in bulk systems [25–29]. While the $5s$ and $5p$ orbitals are fully occupied, the $5d$, $6s$, and $6p$ may not be completely filled and can be probed with spin-polarized STM [30]. Lanthanide atoms such as holmium (Ho) and dysprosium (Dy) with long-living magnetic states have already been used in ESR-STM experiments as local sources of magnetic fields [24,31]. These atoms exhibit an Ising-like ground state that can be sensed by spin-polarized tunneling current. However, according to present knowledge, their large total angular momentum (J) maximally projected along the out-of-plane direction (z) excludes their use as atomic spin qubits because selection rules forbid efficient transitions between the lowest energy states. The challenge is to find an element allowing transitions with variation of the projected total angular momentum $\Delta J_z = \pm 1$ between the ground-state doublet, which maximizes the efficiency of ESR driving. The most intuitive way to attain such configurations is to use atoms possessing an odd number of $4f$ electrons and out-of-plane hard axis of magnetization, favoring a ground state with the lowest $J_z = \pm 1/2$ (with the z -axis perpendicular to the surface) [32]. Alternatively, efficient ESR drive can also be realized in atoms having a ground state expressed by a linear combination of several J_z states [27]. Previous experiments on different substrates [33–35] showed that erbium (Er) and thulium (Tm) have the tendency to assume a configuration with an odd number of $4f$ electrons, namely $4f^{11}$ and $4f^{13}$, respectively. In a suitable ligand environment [36] they exhibit a $J_z = \pm 1/2$ ground state that can allow for quantum coherent operation. A thin layer of magnesium oxide (MgO) provides an excellent decoupling from the metal substrate given its insulating nature and intrinsically low phonon density of states at the low energies of interest [23,37], and, currently, MgO deposited on the silver(100) surface [MgO(100)/Ag(100)] is the only substrate on which ESR-STM is routinely performed. However, whether Er and Tm atoms on this substrate present a suitable ground state for fast and efficient quantum coherent operations is an open question. To this extent, ensemble techniques such as x-ray absorption spectroscopy (XAS) and x-ray magnetic circular dichroism (XMCD) provide a way to obtain accurate information about the ground state of a system by spatial ensemble measurement of a large number of quantum spins simultaneously with precise chemical sensitivity and orbital selectivity [35,38].

In this work, we use XAS and XMCD to characterize the magnetic quantum states of Er and Tm single atoms deposited

on MgO ultrathin films on Ag(100). We address their adsorption sites and the possibility of atomic manipulation using low-temperature STM. Density functional theory (DFT) and atomic multiplet calculations allow us to retrieve the adsorption geometry, electronic structure, magnetic ground state, and magnetization easy-axis of the adatoms. Combining our calculations with the piezoelectric model for ESR-STM [10], we predict Rabi rates up to six times larger than the fastest rates reported for single surface adsorbed atoms and molecules [9,20]. The high Rabi rates are due to the coupling between the radiofrequency (rf) excitation and the large total angular momentum of the lanthanides. These properties, together with the expectedly long coherence time of the $4f$ electron spin [25–27,39], make Er and Tm atoms on MgO(100)/Ag(100) highly promising atomic spin qubits on surfaces.

The manuscript is organized as follows. In Sec. II we present the details about the STM and XAS/XMCD experiments, as well as the atomic multiplet and DFT calculations. In Sec. III the results of the experiments are reported and the predictive model for ESR-STM excitations is described, along with quantitative estimates based on previously reported experimental parameters [10]. Finally, in Sec. IV the results are summarized and conclusions are presented.

II. EXPERIMENTAL AND THEORETICAL DETAILS

A. Scanning tunneling microscope

The STM measurements of Er on MgO(100)/Ag(100) were performed with a home-built STM at a temperature of 4.7 K. The Ag surface was prepared by repeated cycles of Ar⁺ sputtering (ion energy of 0.8 keV) and annealing at 770 K. The MgO thin films were grown by evaporating Mg from a Knudsen cell in a partial pressure of oxygen of 10^{-6} mbar with the sample kept at 770 K, as described in [40]. The growth rate of MgO was estimated to be around 0.1 monolayers (ML) per minute, with a ML defined as a MgO(100) unit cell per Ag(100) atom of the substrate. The sample was cooled down at approximately 30 K/min. Er single atoms were deposited with an e -beam evaporator maintaining the substrate temperature at ~ 10 K and the pressure below 10^{-10} mbar.

The STM measurements of Tm atoms on MgO(100)/Ag(100) were performed on a commercial ultrahigh-vacuum (UHV) LT-STM (RHK Technology) at a temperature of 10 K and a pressure of less than 10^{-10} mbar. Single-crystal, atomically flat Ag(100) was cleaned by several cycles of Ar⁺ ion sputtering (ion energy of 1.2 keV) and annealing at a temperature of around 800 K [40]. Patches of ultrathin (2–3 ML) MgO were grown on top of Ag by magnesium evaporation from a crucible in an oxygen atmosphere (10^{-6} mbar), maintaining the sample at a temperature of 625 K [40]. At these conditions, the growth is about 0.1–0.2 ML per minute. The sample was cooled down gradually to room temperature in about 1 h. Tm atoms were subsequently deposited on the surface at a temperature lower than 20 K. Differently from previous reports [41–43], in all STM images we assume the thinnest MgO patches have a thickness of 2 ML, in line with the more recent definition obtained using conductance measurements on Fe atoms on MgO(100)/Ag(100) [44].

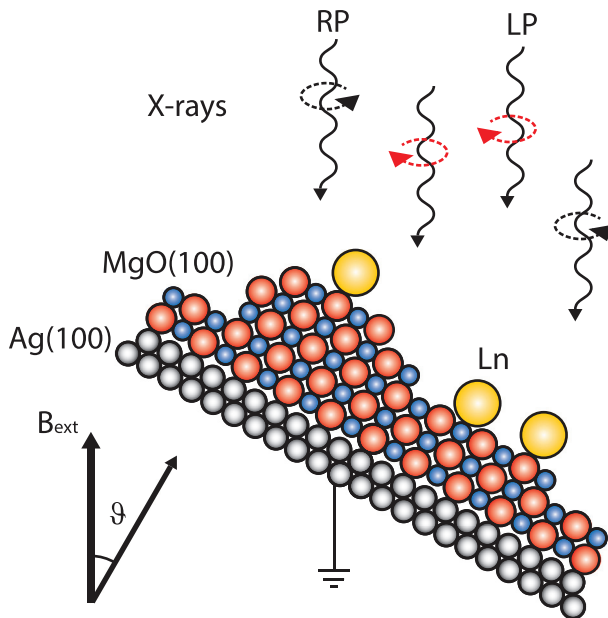


FIG. 1. Schematic of an XMCD experiment of lanthanide atoms (Ln = Er, Tm, yellow spheres) on MgO(100)/Ag(100) (Mg, blue sphere and O, red sphere). The lanthanide adatoms bind to the MgO surface on two possible adsorption sites, namely on oxygen and on bridge, as discussed in the text. The external magnetic field is always applied parallel to the direction of the x-rays while the whole sample is rotated by an angle ϑ . Right (RP) and left (LP) circularly polarized x-rays are represented by black and red circular arrows, respectively.

B. X-ray magnetic circular dichroism

XAS and XMCD measurements of the two lanthanide adatoms on MgO(100)/Ag(100) were performed at the EPFL-PSI X-Treme beamline [45]. The samples were prepared *in situ* by growing approximately 4 ML of MgO(100) on Ag(100) with the method explained above. A thicker MgO layer is used in order to obtain a full coverage of the Ag surface. This avoids the introduction of a different type of lanthanide atom adsorbed on bare Ag, which would increase the complexity of the interpretation of the XMCD data. The lanthanide single atoms were deposited at a temperature lower than 10 K and subsequently studied using synchrotron light. The measurements were performed at low temperature (2.5 K) using right (RP) and left circularly polarized light (LP) from the synchrotron source, with the photon beam, parallel to the magnetic field, either at normal ($\vartheta = 0^\circ$) or at grazing ($\vartheta = 60^\circ$) incidence. A schematic representation of the experiment is reported in Fig. 1. The XAS spectra are the polarization-integrated absorption signal, calculated as the sum of the RP and LP signals amplitude, while the XMCD is obtained as the difference between RP and LP and is proportional to the spin and orbital magnetic moment of the probed shell projected onto the incident x-ray beam. The XAS/XMCD spectra were acquired at the $M_{4,5}$ edges of the lanthanide atoms, corresponding to the resonant excitation of an electron from the $3d$ to the $4f$ shell. This allows one to probe the occupation of the $4f$ shell and its orbital and spin magnetic properties.

C. Atomic multiplet calculations

To interpret the XMCD data, we compared the experimental spectra with simulated ones obtained from atomic multiplet calculations using the QUANTY code [46]. These include electron-electron interactions, the spin-orbit coupling, the crystal field, and the external magnetic field (B_{ext}). We approximated the crystal field using a point-charge model as described in previous works [24,38] with coordinates of the point charges determined by DFT calculations, as described in the next section (see also Tables II–V for details of the crystal field employed). The electron-electron interaction and spin-orbit coupling are included by rescaling the atomic parameters obtained from full-electron Cowan's atomic structure code [47]. The Coulomb interactions were reduced to 85% in order to match the experimental spectra [35], while no rescaling was applied to the spin-orbit coupling. Finally, we applied a Lorentzian broadening with a full width at half maximum of $\Gamma = 1.75$ and 1.5 eV to match the line broadening for the Er and Tm spectra, respectively.

D. Density functional theory

To obtain the crystal field strength and geometry, we performed density functional theory (DFT) calculations using QUANTUM ESPRESSO (V 6.5) [48] with projector-augmented wave (PAW) pseudopotentials from the SSSP Library [49]. The plane-wave basis was expanded using a kinetic cutoff of 60 Ry for the wave functions and 600 Ry for the charge density. Integration of the Brillouin zone was performed on a $3 \times 3 \times 1$ regular k -grid. In all calculations, the $4f$ electrons of the lanthanide were treated as valence electrons, and the calculations were performed including electron spin-polarization. Our system consists of a 3×3 lateral supercell ($a = 4.21$ Å) of 4 ML of MgO to which the adatom was added either on oxygen or bridge sites and the system was relaxed until all forces are below 0.001 Ry/ a_0 . The coordinates of the point charges obtained from DFT together with their ionic values were used as input for the crystal field in the atomic multiplet calculations (Tables II–V).

Differently from previous works [38,41], here we do not include the Ag(100) substrate underneath the MgO(100) in our calculations. Even if the presence of the metal substrate is expected to have an impact on the electronic structure of the adsorbed atoms, the impact on the geometry is typically rather small, with the main effect being the influence on the bond length to the underneath oxygen(s) [41]. Calculations on Dy atoms on MgO/Ag(100) [41] indicate that the variations of this bond length are rather small and they mainly affect the energy level separation, without significantly altering the hierarchy of the states or the magnetic moment of the ground state derived from the atomic multiplet calculations.

III. RESULTS AND DISCUSSION

A. Adsorption sites

Holmium and dysprosium atoms have been reported to adsorb on oxygen or bridge sites of the MgO(100) lattice. Both sites distinguish themselves by the lateral position of the adatoms with respect to the MgO lattice, which is accompanied by a difference in apparent height [41–43]. The STM

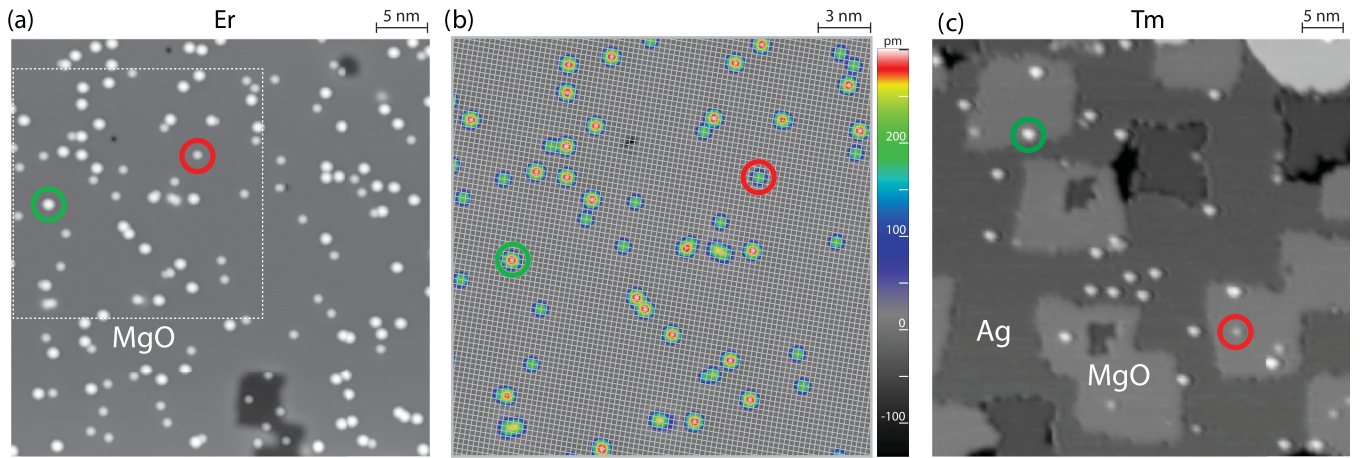


FIG. 2. (a) Constant current STM image of individual Er atoms on MgO(100)/Ag(100). Red (green) circles indicate Er atoms on O (bridge) adsorption sites. Erbium coverage: 0.8% ML ($V_t = -200$ mV, $I_t = 200$ pA, $T = 5$ K). (b) Zoom into the region outlined by the dashed square in (a). A grid extracted from an atomically resolved STM image acquired on MgO is superimposed onto the image to identify the Er adsorption sites. (c) Constant current STM image showing individual Tm atoms with two apparent heights on MgO(100)/Ag(100) (square patches) and with one apparent height on the Ag(100) substrate. Magnesium oxide thicker than 2 ML appears as darker areas in the STM image. In the red (green) circle we indicate a Tm atom on the O (bridge) adsorption site. Thulium coverage: 0.2% ML ($V_t = 200$ mV, $I_t = 100$ pA, $T = 10$ K).

image in Fig. 2(a) shows individual Er atoms adsorbed on a 2 ML MgO island on Ag(100). Two species are distinguishable from their apparent height (225 ± 10 and 300 ± 10 pm). Similar to Ho and Dy, no features have been observed in differential conductance spectra for $V_t < 300$ meV regardless of their adsorption site [23,41,43]. Figure 2(b) shows a zoom into the marked area together with an overlaid grid extracted from an atomically resolved image of MgO. The registry of the grid is chosen such that all atoms with low apparent height are on the crossings. All atoms with the larger apparent height are found on the two possible half-intersections between two grid crossings. This unequivocally identifies the fourfold symmetric adsorption site with the species with lower apparent height, and the twofold bridge site with the larger one. Co-deposition of Er with atomic markers, such as Co or Ho, for whom the adsorption site is known, confirms that the fourfold symmetric site is the oxygen site [43]. Statistical analysis carried out on 2 ML MgO indicates that $41\% \pm 4\%$ ($59\% \pm 4\%$) of the Er atoms are adsorbed on O (bridge) sites. Conversely, adsorption on O is predominant on 3 ML, following the same trend observed for Ho [42] and Dy [41]. For Tm, a detailed lateral adsorption site analysis was not carried out; however, also for this element, two species are clearly distinguished by their apparent heights of about 130 and 280 pm [Fig. 2(c)]. Assuming that Tm behaves as Ho, Dy, and Er, the Tm species with apparent height close to that of the other three lanthanides adsorbed on the bridge site are assigned to bridge sites, while the species with the lower apparent height are assigned to the O adsorption site.

Different adsorption sites create a different crystal field acting on the magnetic states of the adsorbed atom. We note that Ho and Dy atoms can reversibly be switched between the two sites by voltage pulses [42,43]. Without carrying out an extensive study of the adsorption site manipulation, we find also for the two elements studied here that they can be moved between the two adsorption sites by applying voltage pulses of more than 600 mV.

B. Magnetic level scheme

In Fig. 3 we show the XAS/XMCD spectra over the M_5 edge of Er and Tm. For both elements we focus on the M_5 edge as the M_4 edge is much weaker, as is generally observed for elements at the end of the lanthanide series [23,38]. For both Er and Tm, the M_5 XAS and XMCD present a marked angular dependence that indicates large magnetic anisotropy. In contrast to Dy [24] and Ho [23] on the same substrate, Er and Tm present a larger XMCD signal in grazing incidence, typically suggesting an easy-plane anisotropy parallel to the surface [23,41,50]. The Er spectra [Fig. 3(a)] are typical of a $4f^{11}$ occupancy [35]. The Tm spectra [Fig. 3(b)], on the other hand, show two main peaks which, based on previous studies [35,51], can be ascribed to the coexistence of $4f^{12}$ and $4f^{13}$ electronic configurations. The lower energy peak (1454 eV) is attributed to the $4f^{13}$ species and presents a larger XAS intensity, as well as a pronounced XMCD anisotropy, with the intensity in grazing incidence (GI) roughly three times larger than in normal incidence (NI). The higher energy peak (1458 eV) is ascribed to the $4f^{12}$ species and shows no angular dependence.

To interpret our results, we fit the data with spectra simulated by atomic multiplet calculations, taking into account the different adsorption sites and $4f$ occupations. For Er we consider two species, both $4f^{11}$, once on O and once on the bridge, while for Tm we consider four species, $4f^{12}$ and $4f^{13}$, each on the two adsorption sites. All six species show a very strong in-plane anisotropy (see Appendix B, Figs. 8 and 9). The relative abundances of the various species are the only fit parameters.

Our fit for Er identifies a majority of Er atoms on O adsorption sites, as reported in Table I. The high uncertainty in the proportion of O sites with respect to bridge sites is due to their similar spectral shape. The fit reproduces the XAS in both directions, as well as the XMCD in GI; see Fig. 3(a). However, the simulated XMCD in normal incidence is

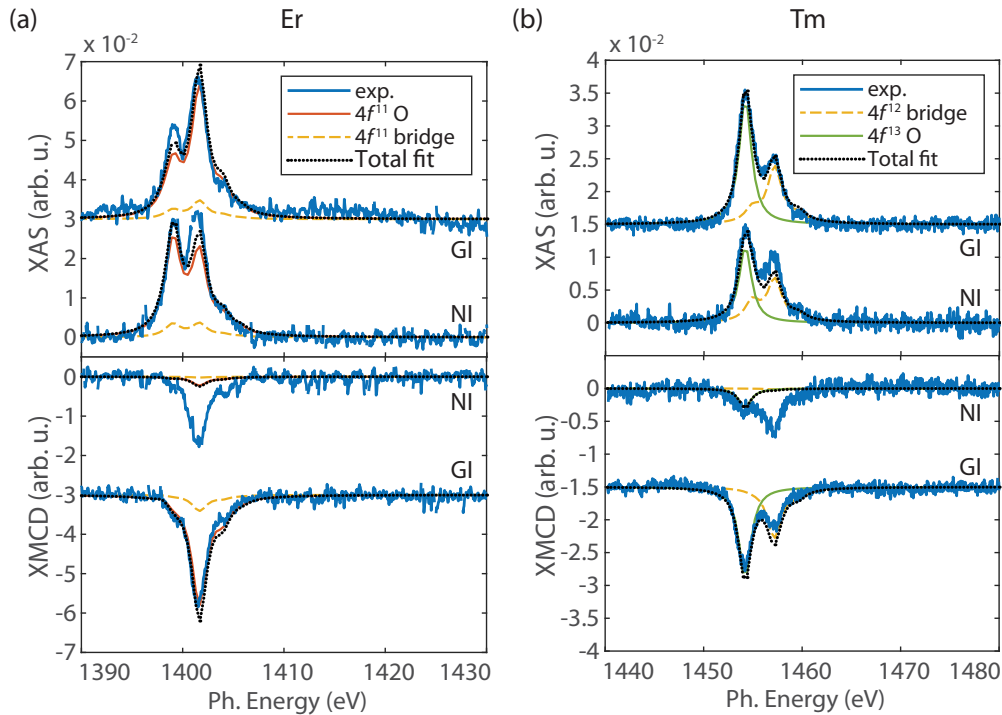


FIG. 3. (a) XAS and XMCD spectra at the M_5 edge of Er on MgO(100)/Ag(100) at normal (NI) and grazing incidence (GI). The experiments are reported as blue lines. Atomic multiplet calculations with $4f^{11}$ on O (red), $4f^{11}$ on bridge (dashed yellow) species yield the total fit (dotted black line). The fitting parameters with their confidence intervals are reported in Table I. XAS and XMCD in grazing incidence are shifted up and down by 0.03 arb. units, respectively (MgO thickness: 3.9 ML, $B = 6.7$ T, $T = 2.5$ K). (b) XAS and XMCD at the M_5 edge of Tm on MgO(100)/Ag(100). Fits of the data using atomic multiplet calculations including two species ($4f^{13}$ on O, green; $4f^{12}$ on bridge, dashed yellow) are shown together with the total fit (dotted black line); the $4f^{12}$ on O and $4f^{13}$ on bridge spectra are omitted. The spectra in grazing incidence are shifted up and down by 0.015 arb. units, respectively (MgO thickness: 4.3 ML, $B = 6.7$ T, $T = 2.5$ K).

noticeably smaller than the experimental value. The Tm fit suggests that essentially two species are present on the surface, namely $4f^{13}$ on O and $4f^{12}$ on the bridge, with a majority of $4f^{13}$ on O; see Table I. With such an ensemble composition, the fit [Fig. 3(b)] reproduces the XAS in both directions, as well as the XMCD in GI and the XMCD in NI for the $4f^{13}$ species (1454 eV). Only the $4f^{12}$ XMCD peak (1458 eV) in normal incidence cannot be accounted for.

The higher abundancy of the O site is in agreement with DFT results, which indicate that the O site has 280 (320) meV higher binding energy than the bridge site for Er (Tm) on the MgO thickness of 4 ML used in the XMCD experiment. The results obtained for atoms on this MgO thickness should not be compared to the STM data acquired on 2 ML, but rather to the ones on 3 or more ML, which show preferential adsorption on O for Ho, Dy, and Er [23,41,43]. The $4f^{12}$ occupancy for

the bridge site for Tm can be rationalized by the adsorption geometry: on this site, Tm is coordinated with two oxygen atoms, and this can favor a lower occupation of the $4f$ orbitals [35].

The spectral features in NI XMCD that are missing in our single atom fits can be reproduced introducing Er and Tm dimers as additional surface species (see Fig. 10). For the employed coverages of 1.4% of ML for Er and 1.3% for Tm, one expects the presence of a small fraction of dimers from rare-earth adsorption on surfaces [33,52,53]. Although the charge transfer on MgO is different from the one on graphene, the rare-earth atoms likely possess also on MgO the large direct capture areas leading to dimer formation. The coverages used in the STM experiments are with 0.8% and 0.2% ML significantly lower and therefore the abundance of dimers is low; however, in Fig. 2(b), one can identify three objects with an elongated footprint that are likely dimers. The abundance of atoms in the form of dimers obtained from the fit (22% for Er and 14% for Tm) is consistent with previous works [53]. In addition, the proportion of O and bridge species does not change significantly when including dimers in the model (see Table VI). Therefore, the presence of dimers does not alter the conclusions we draw for single atoms, i.e., they prefer the O site, and their spectral features are well reproduced.

We now analyze the level scheme of the lowest multiplets for both rare-earth elements. Among the two adsorption sites, O is the one with the highest symmetry and presents a well-defined quantization axis along the out-of-plane direction z

TABLE I. Abundancies and relative confidence intervals obtained from the fit of Er and Tm XAS/XMCD spectra with the spectra calculated with atomic multiplet calculations.

Er fit		Tm fit	
$4f^{11}$ O	87 $^{100}_{66}$ %	$4f^{13}$ O	71 $^{72}_{70}$ %
$4f^{11}$ bridge	13 $^{34}_0$ %	$4f^{13}$ bridge	0%
		$4f^{12}$ O	1 7_0 %
		$4f^{12}$ bridge	28 $^{34}_{22}$ %

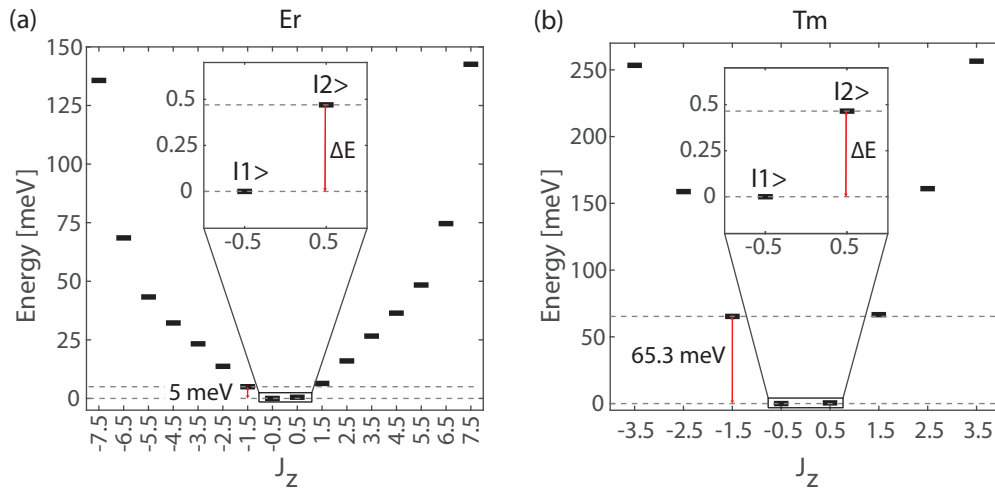


FIG. 4. Energy level diagrams of Er (a) and Tm (b) adsorbed on the O sites of MgO(100)/Ag(100) showing the lowest atomic multiplet. The out-of-plane external magnetic field (6.7 T) splits the lowest doublet ($|1\rangle$ and $|2\rangle$) by the Zeeman energy ΔE shown in the zoomed region. The second excited state is separated from the ground state by the zero-field splitting.

[24]. Applying an out-of-plane magnetic field preserves an almost cylindrical symmetry, hence J_z is a good quantum number to describe the quantum states of the atoms. Therefore, we focus our analysis on the $4f^{11}$ Er and $4f^{13}$ Tm adsorbed on the O site. These species present a lowest atomic multiplet with a total angular momentum $\mathbf{J} = 15/2$ and $7/2$, respectively, and a large in-plane anisotropy. In contrast to Dy [24] and Ho [31] on the O site of MgO(100)/Ag(100), which present out-of-plane anisotropy, the in-plane anisotropy of Er and Tm leads to a minimization of the projection of \mathbf{J} in the direction perpendicular to the surface, i.e., J_z . The marked difference in magnetic anisotropy between the lanthanides is due to the magnetic ground state associated with the $4f$ charge distribution that minimizes the electrostatic repulsion with the surrounding charges [34,36]. For adsorption on top of oxygen, an oblate charge distribution is expected to be energetically favorable [36]. In the case of $4f^9$ and $4f^{10}$ (Dy and Ho, respectively), this charge density corresponds to a ground state with the largest J_z . On the other hand, for $4f^{11}$ and $4f^{13}$ (Er and Tm, respectively) the oblate charge density is obtained with the minimum J_z , in particular $J_z = \pm 1/2$ [36]. Indeed, the atomic multiplet calculations indicate that the quantum level structure is characterized by doubly degenerate states with half-integer values of J_z , with a ground doublet having $J_z = \pm 1/2$. This kind of system is an optimal platform to perform ESR spectroscopy [14]. When an external magnetic field is applied, the ground doublet $|1\rangle$ and $|2\rangle$ splits by the Zeeman energy (ΔE) (Fig. 4) and it is possible to excite ESR transitions between these two states, effectively realizing a spin qubit. The high anisotropy of both systems has the effect of increasing the energy separation between the ground doublet ($J_z = \pm 1/2$) and the first excited doublet ($J_z = \pm 3/2$) (Fig. 4). This energy separation is more than 5 meV for Er and 65 meV for Tm. This difference in the energy splitting can be attributed to two factors. First, the spread of the magnetic states over the total magnetic anisotropy energy is larger for Er (16 states) than Tm (8 states). Second, the $4f^{13}$ filling of Tm is associated with a more pronounced charge anisotropy, whose electrostatic interaction with the underneath oxygen induces

a larger energy difference between magnetic states. For both elements, these energy splittings are significantly larger than ΔE , even at high magnetic field ($\Delta E = 0.47$ meV for both elements at 6.7 T). Indeed, at the experimental temperature (< 10 K) the second excited state is not thermally occupied, and it is too high in energy to be excited by the radiofrequency (carrying photons with energy of the order of hundreds of μeV). This large level splitting isolates an effective two-level system $|1\rangle$, $|2\rangle$, leading to a reduction of the so-called qubit leakage, i.e., the outflow of the qubit state from the two-level subspace, which negatively impacts the performance of most qubit systems [54]. When the magnetic field is applied at an arbitrary angle, however, it causes a level mixing and J_z is no longer a good quantum number. Nevertheless, due to the large zero-field splitting, the system can still be treated as a two-level system with a ground-state doublet split by ΔE .

These properties indicate the potential of Er and Tm atoms on the O site of MgO(100)/Ag(100) as qubit candidates with suitable properties for ESR-STM experiments. Using the eigenenergies and the multielectron wave function of the $4f$ states determined by the atomic multiplet calculations, we estimate the angular and field-dependent frequency $\Delta E/h$ of the ESR-STM transitions; see Fig. 5. The transition frequency increases linearly with \mathbf{B}_{ext} [Figs. 5(a) and 5(b)]. In contrast to an isotropic spin-1/2 system [dashed lines in Figs. 5(c) and 5(d)], Er and Tm atoms exhibit a strong angular dependence of the ESR frequency at constant field. This behavior stems from the large magnetic anisotropy that favors the in-plane alignment of \mathbf{J} . Both Er and Tm show similar field-dependent splitting at 0° due to their same $J_z = \frac{1}{2}$ ground state and comparable g -factor. Conversely, when the field is applied at an angle from the normal, the larger magnetic moment of Er gives larger energy splitting compared to Tm. Considering the vector $\langle \mathbf{J} \rangle = (\langle \hat{J}_x \rangle, \langle \hat{J}_y \rangle, \langle \hat{J}_z \rangle)$ as a function of the external magnetic field angle, our atomic multiplet calculations show that \mathbf{J} does not follow \mathbf{B}_{ext} when it is applied at an angle different from 0° or 90° . Specifically, the atom magnetic moment aligns more easily along the in-plane component of the magnetic field, resulting in an angle δ between the external

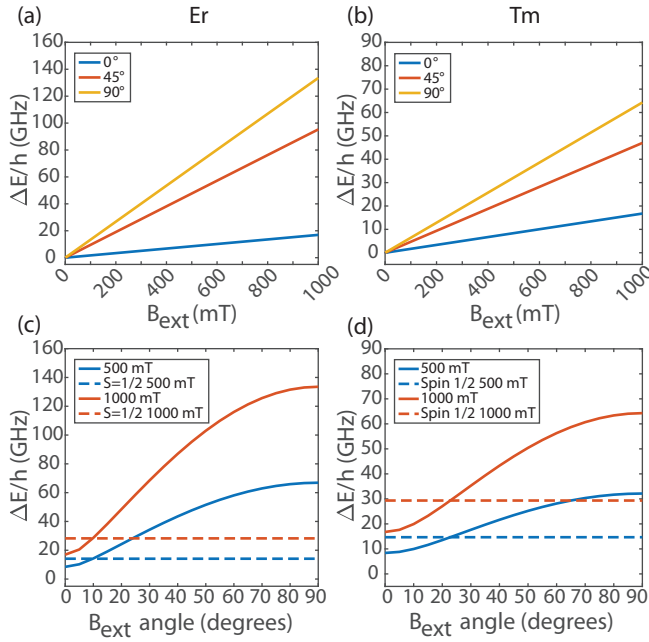


FIG. 5. Predicted Zeeman energy splitting calculated with atomic multiplet calculations for Er (a) and Tm (b) as a function of B_{ext} at 0° (blue line), 45° (red line), and 90° (yellow line). Predicted Zeeman splitting for Er (c) and Tm (d) as a function of the external magnetic field angle at 500 mT (blue solid line) and 1000 mT (red solid line) in comparison with an isotropic spin $1/2$ system (dashed lines).

field and the atom magnetization that can deviate up to 75° and 60° from the field direction for Er and Tm, respectively, as reported in Fig. 6. This feature has to be considered when choosing the spin-coordinate system to describe the coherent evolution of the quantum state. In addition, when measuring the quantum state of the atom through spin-polarized current, the noncollinearity between the magnetization of the probing electrode (the tip) and that of the atom may affect the intensity of the signal, as will be discussed in the following section.

C. Model for ESR-STM excitations

To predict the Rabi rate of the lanthanide atoms under the drive of the tip, we combine the detailed description of the

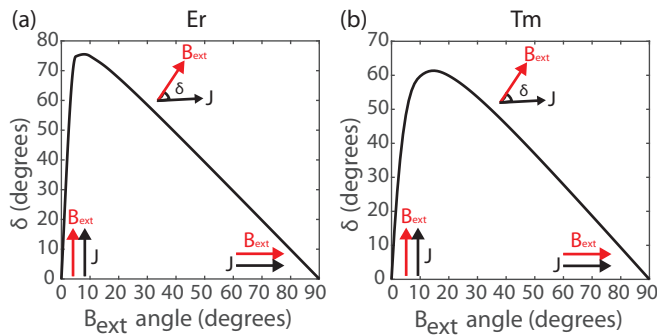


FIG. 6. Predicted angle δ between B_{ext} and the atom J as a function of the magnetic field angle for Er (a) and Tm (b). A schematic of the magnetic field alignment (red arrow) and the atom J (black arrow) is reported alongside the graph.

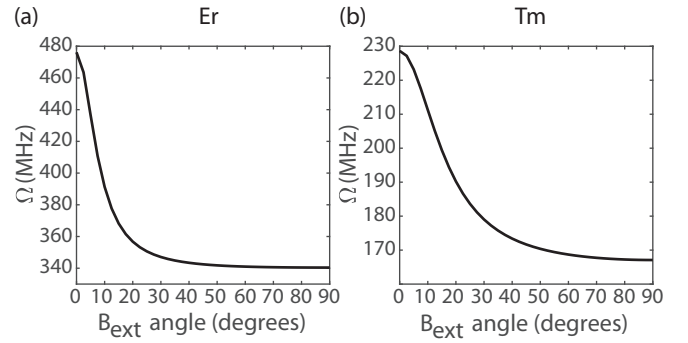


FIG. 7. Predicted Rabi rate as a function of the external magnetic field angle for Er (a) and Tm (b) at a driving rf voltage of 250 mV.

quantum states obtained from the atomic multiplet calculations with a previously developed ESR-STM model [10,55–57]. The Rabi rate Ω can be estimated using the piezoelectric coupling model [10,58]:

$$\Omega = \left| \frac{\mu_B}{\hbar} \Delta z_{\omega_{\text{rf}}} \frac{d\mathbf{B}_{\text{eff}}}{ds} \langle 2 | \hat{L} + 2\hat{S} | 1 \rangle \right|,$$

where μ_B is the Bohr magneton, \hbar is the reduced Planck constant, $\langle 2 | \hat{L} + 2\hat{S} | 1 \rangle$ is the transition matrix element, B_{eff} is the effective magnetic field calculated as the vector sum between the tip and B_{ext} , s is the distance between the atom and the tip apex, thus $\frac{dB_{\text{eff}}}{ds}$ is the effective field gradient between the atom and the tip. Finally, $\Delta z_{\omega_{\text{rf}}}$ is the atom displacement induced by the rf field. For the evaluation of Ω , we use a typical value of $\Delta z_{\omega_{\text{rf}}}$, estimated both for hydrogenated titanium on bridge sites (TiH) and iron on O (Fe) [10], of the order of 0.4 pm at an rf voltage amplitude of 250 mV. As $\frac{dB_{\text{eff}}}{ds}$ is tip-dependent and varies with s , we take the value of 2 T/nm, as evaluated in [10]. Finally, we calculate the transition matrix elements between the eigenstates resulting from our atomic multiplet calculations. This term shows a dependence on the angle of B_{ext} while it is essentially constant with the magnetic field amplitude.

As shown in Fig. 7, the Rabi rates calculated for Er and Tm can reach up to 480 and 230 MHz, respectively, when the magnetic field is applied out-of-plane. These values are a few times larger than the highest values reported so far for TiH [9,10] and two orders of magnitude larger than for Fe atoms [10]. These fast Rabi rates are due to the amplitude of the transition matrix element, which is, respectively, six and three times larger than TiH [10], due to the larger total magnetic moment of these lanthanides. In addition, the $J_z = \pm 1/2$ doublet of Er and Tm allows a larger ESR drive compared to Fe for which the driving mechanism stems from a weak longitudinal transition connecting the $S_z = \pm 2$ states [6,10].

In both systems, the rates are maximum when the field is oriented out-of-plane, and they show a reduction of about 30% when rotating the field towards the in-plane direction. We can rationalize this result by considering the angular dependence of the transition matrix element. The \hat{J} operator connects the states separated by magnetic quantum numbers $\Delta m_J = \pm 1, 0$. When a magnetic field is applied in the out-of-plane direction, the ground doublet is described by pure states with $J_z = \pm 1/2$. The $\Delta J_z = 1$ matches the selection rule

for the transition and therefore the Rabi rate is maximum. In the general situation in which the magnetic field is applied off-normal, the ground doublet is characterized by a highly admixed J_z state resulting in a ΔJ_z larger than 1. In this case, our atomic multiplet calculations indicate that the ESR transition is still allowed due to the large fraction of the $J_z = \pm \frac{1}{2}$ states present in the mixed ground doublet. This mechanism was also observed in previous reports on lanthanide molecular spins [27]. It is worth noting that, even though $\frac{dB_{\text{eff}}}{ds}$ and $\Delta z_{\omega_{\text{rf}}}$ were not measured for these specific systems, the calculated Rabi rate scales linearly with these quantities, allowing for an easy extrapolation. Our model can be further extended to predict the intensity of the ESR-STM signal, as described in Appendix D.

The large Rabi rates predicted by our model, combined with the expected long coherence time for lanthanides, may lead to large qubit quality factors of these atoms. In bulk oxides, lanthanides show an electron spin coherence time of up to 1 s [26,28,29]. However, due to the scattering with Ag electrons tunneling through the ultrathin MgO layer, Er and Tm on MgO(100)/Ag(100) are expected to exhibit a much shorter coherence time. In addition, T_2 is further reduced due to the scattering with the tunneling electrons in ESR-STM experiments. Under experimental conditions leading to a coherence time T_2 limited by the tunneling current, we have $T_2 \approx e/(r_2 I)$ [59], where r_2 is the probability for an electron to cause a decoherence event, e is the electron charge, and I is the sum of the dc and rf current. For TiH and Fe, it was shown that every tunneling electron causes a decoherence event, i.e., $r_2 \approx 1$ [10]. In $4f$ atoms on MgO(100)/Ag(100), the tunneling current effectively interacting with the unpaired electron spins is typically reduced by a factor of 10 with respect to $3d$ atoms, as estimated from the amplitude of the telegraph signal observed in spin-polarized STM experiments [24,31,44,50]. Hence, we expect r_2 to be reduced by a factor 10. Within this assumption, we expect Er and Tm to offer a qubit quality factor up to 50 and 25 times higher than that of TiH, respectively. This would represent a remarkable step forward with respect to present single transition-metal atoms, and it may allow one to implement sequences of controlled quantum operations.

IV. CONCLUSIONS

By addressing the surface adsorption with STM and combining XMCD measurements with DFT and atomic multiplet calculations, we were able to identify Er and Tm as candidate surface spin qubits. Our results indicate that when adsorbed on the O site of MgO(100)/Ag(100), these atoms are characterized by a strong in-plane anisotropy that favors a doubly degenerate ground state for which transitions with $\Delta m_J = \pm 1, 0$ are possible. This ground state makes Er and Tm particularly suitable to be used as spin qubits in ESR-STM experiments, for which we expect a Rabi rate of up to 480 MHz in standard experimental conditions. The predicted values stand on the values of B_{eff} and $\Delta z_{\omega_{\text{rf}}}$ that have been adapted from previous experiments and need to be verified in dedicated ESR-STM experiments conducted on lanthanides. For $\Delta z_{\omega_{\text{rf}}}$ we expect a value similar to that of TiH or Fe. However, the charge transfer to the metal substrate, present

in most surface-adsorbed lanthanide atoms [38], may lead to an increased electric dipole and improve the oscillation driven by the rf field. As for B_{eff} , this value depends on the exchange coupling and the dipolar interaction between the tip and the atom [10]. For lanthanides the exchange coupling may be weaker than for TiH or Fe due to the shielding effect of the outer orbitals on the $4f$. In turn, the dipolar interaction should be larger due to the larger total magnetic moments of these atoms, partially compensating for the reduced exchange interaction with the tip. Finally, it is known that TiH and Fe require different gradient directions due to their different excitation mechanism [10]. This complicates the measure of both atoms with a single tip. In contrast to Fe, in Er and Tm the x and y components of the angular momentum matrix elements are nonzero. This is because Fe has an Ising-like $S = \pm 2$ ground-state doublet [10] while Er and Tm are $J_z = \pm 1/2$. For this reason, Er and Tm present an excitation mechanism similar to TiH, thus we predict that a tip giving a large ESR signal on TiH should also work well for Er and Tm.

In addition to their suitable electron spin properties, these two elements naturally possess a nontrivial nuclear spin. Specifically, Tm has a single natural isotope characterized by a spin $\frac{1}{2}$ nucleus, while all Er natural isotopes have zero nuclear spin except for ^{167}Er , with a natural abundance of 22.93% and a nuclear spin of $7/2$. The nuclear spin of these elements can be exploited to perform two-qubit calculations on a single atom or to store quantum states on the nuclear spin.

ACKNOWLEDGMENTS

This work was supported by the Institute for Basic Science (Grant No. IBS-R027-D1). The authors are grateful to A. J. Heinrich for careful reading of the manuscript and valuable comments to this work. The authors also thank Y. Bae for useful discussions.

APPENDIX A: POINT CHARGE MODEL

In Tables II–V we present the coordinates of the point charges obtained from DFT together with their ionic values, which were used as input for the crystal field in the atomic multiplet calculations.

TABLE II. Charges and positions of the ions used for calculating the point-charge model for atomic multiplet calculations in Er on O.

Ion	Charge	d_{\perp} (pm)	d_{\parallel} (pm)
O (underneath)	$-2e$	221.6	0
Mg (second nearest neighbors)	$+2e$	263.2	218.0
O (third nearest neighbors)	$-2e$	262.0	298.4

TABLE III. Charges and positions of the ions used for calculating the point-charge model for atomic multiplet calculations in Tm on O.

Ion	Charge	d_{\perp} (pm)	d_{\parallel} (pm)
O (underneath)	$-2e$	223.5	0
Mg (second nearest neighbors)	$+2e$	262.2	217.0
O (third nearest neighbors)	$-2e$	261.2	298.4

TABLE IV. Charges and positions of the ions used for calculating the point-charge model for atomic multiplet calculations in Er on bridge.

Ion	Charge	d_{\perp} (pm)	d_{\parallel} (pm)
O (bridge)	$-2e$	214.0	141.4
Mg (second nearest neighbors)	$+2e$	249.7	161.9

TABLE V. Charges and positions of the ions used for calculating the point-charge model for atomic multiplet calculations in Tm on bridge.

Ion	Charge	d_{\perp} (pm)	d_{\parallel} (pm)
O (bridge)	$-2e$	213.5	141.4
Mg (second nearest neighbors)	$+2e$	249.6	161.9

APPENDIX B: CALCULATED XAS/XMCD FOR INDIVIDUAL SPECIES

In Figs. 8 and 9 we present the XAS and XMCD spectra simulated with atomic multiplet calculations of the Er and the Tm species, respectively, which were used to fit the data shown in Fig. 3.

APPENDIX C: FIT OF XAS/XMCD INCLUDING DIMERS

In Fig. 10 we present XAS and XMCD spectra at the M_5 edge of Er and Tm on MgO(100)/Ag(100). In addition, Table VI displays the abundancies of the species with their confidence intervals as obtained from the fit.

APPENDIX D: ESTIMATION OF THE INTENSITY OF THE ESR-STM SIGNAL

The intensity of the ESR-STM signal is given by the change in the spin-polarized tunneling current due to the rotation of the magnetic moment of the atom projected on the

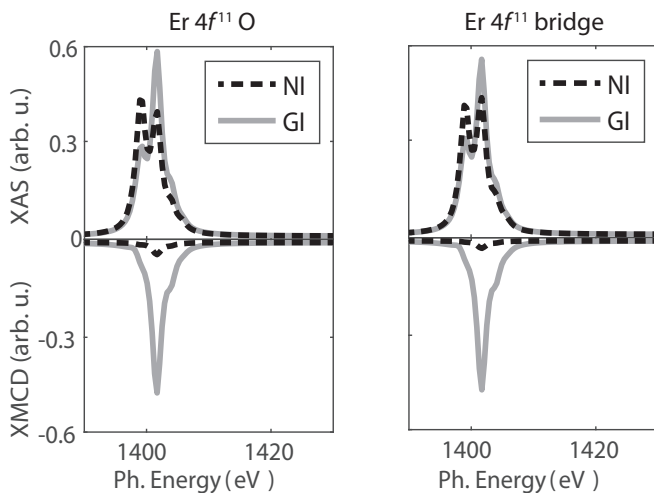


FIG. 8. XAS and XMCD spectra in NI and GI simulated with atomic multiplet calculations of the Er species used in the fit in Fig. 3(a) and Table I.

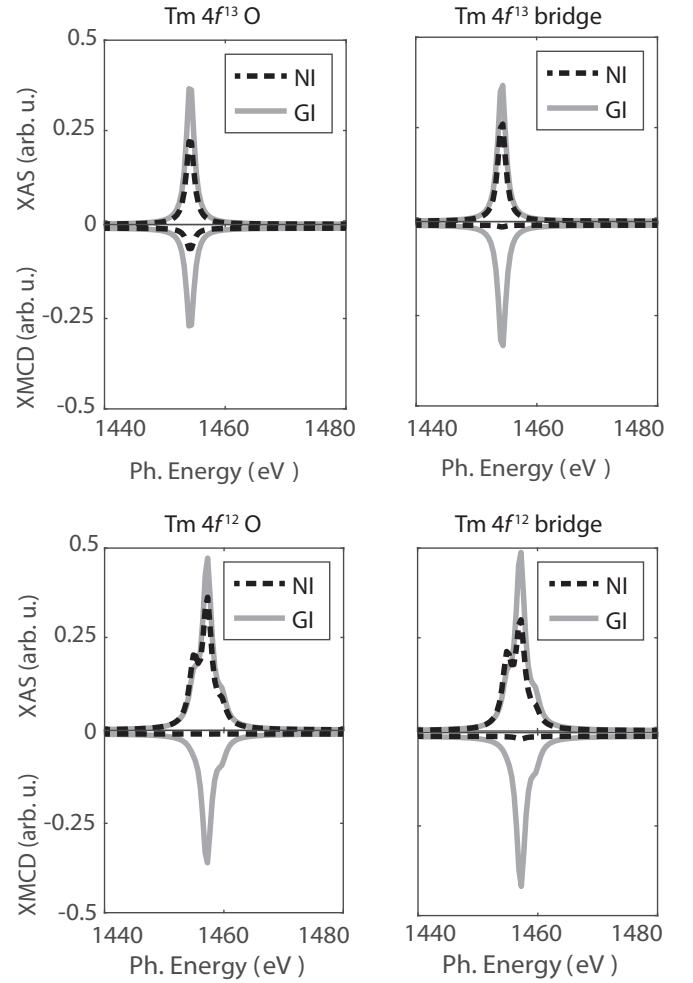


FIG. 9. XAS and XMCD spectra in NI and GI simulated with atomic multiplet calculations of the Tm species used in the fit in Fig. 3(b) and Table I.

tip magnetization axis [6,10]. In this appendix, we estimate the ESR-STM signal normalized at the dc set point current ($\Delta I/I_{dc}$) at the resonant frequency and neglecting the offset due to STM junction conductance nonlinearities [10,55,56],

$$\frac{\Delta I}{I_{dc}} = a_{\text{TMR}}^* \frac{1}{1 + (\Omega^2 T_1 T_2)^{-1}}.$$

In this model, the relative intensity of the excitation depends on four parameters, namely (i) the effective amplitude of the tunneling magnetoresistance a_{TMR}^* ; (ii) the Rabi rate Ω , (iii) the relaxation time T_1 , and (iv) the coherence time T_2 . We estimated the Rabi rate in Sec. III C, while we will make further assumptions on a_{TMR}^* , T_1 , and T_2 based on previous experiments on single magnetic atoms on thin layers of MgO [10,24,31,44,50,59,60]. To evaluate a_{TMR}^* at arbitrary magnetic field angles, we consider the generalized polarization function [10] $\hat{P} = P\vec{\sigma} = P(\sigma_1, \sigma_2, \sigma_3)$, where σ_i are the Pauli matrices for a spin-1/2 system and $P = |\langle \hat{J} \rangle| = \sqrt{\langle \hat{J}_x \rangle^2 + \langle \hat{J}_y \rangle^2 + \langle \hat{J}_z \rangle^2}$ is the magnitude of the polarization. In our model, P depends on the external magnetic field angle and intensity, and it is smaller than the magnitude of the

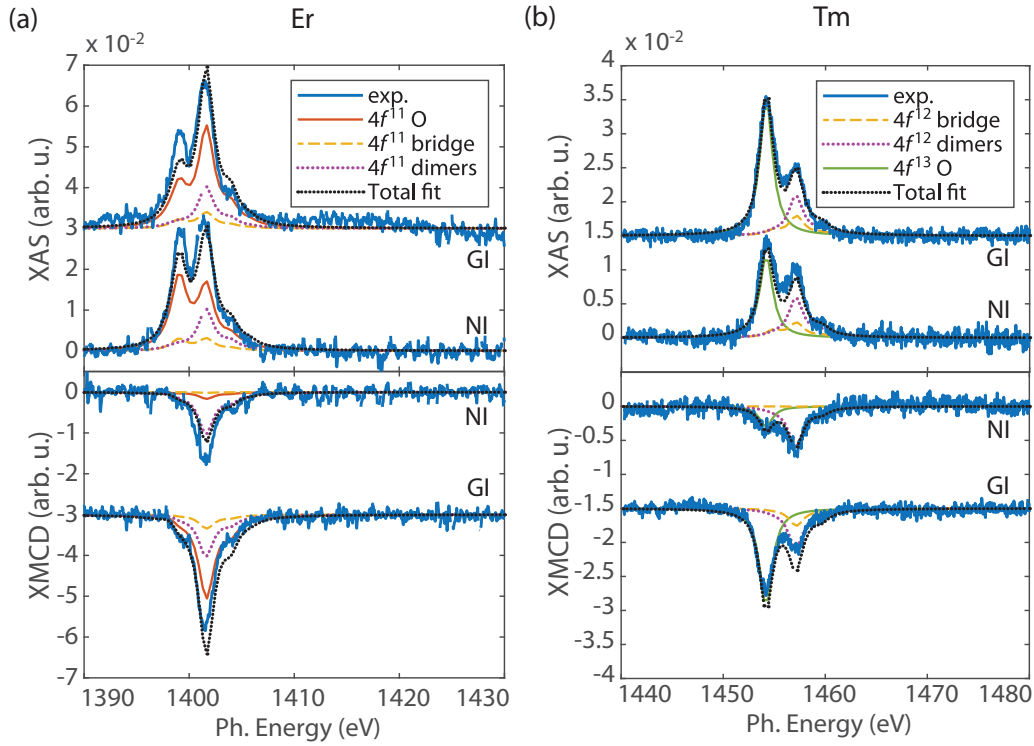


FIG. 10. (a) XAS and XMCD spectra at the M_5 edge of Er on MgO(100)/Ag(100) at normal (NI) and grazing incidence (GI). The experiments are reported as blue lines. Atomic multiplet calculations with $4f^{11}$ on O (red); $4f^{11}$ on bridge (dashed yellow), and $4f^{11}$ dimer (dotted purple) species yield the total fit (dotted black line). The fitting parameters with their confidence intervals are reported in Table VI. XAS and XMCD in grazing incidence are shifted up and down by 0.03 arb. units, respectively (MgO thickness: 3.9 ML, $B = 6.7$ T, $T = 2.5$ K). (b) XAS and XMCD at the M_5 edge of Tm on MgO(100)/Ag(100). Fits of the data using atomic multiplet calculations including three species ($4f^{13}$ on O, green; $4f^{12}$ on bridge, dashed yellow; and $4f^{12}$ dimers, dotted purple) are shown together with the total fit (dotted black line). The spectra in grazing incidence are shifted up and down by 0.015 arb. Units, respectively (MgO thickness: 4.3 ML, $B = 6.7$ T, $T = 2.5$ K). We model dimers for both elements assuming an isotropic behavior to take into account the expected distribution of their angular orientations on the surface.

total angular momentum $\sqrt{J(J+1)}$. Using this formulation, we can treat the system as an ideal two-level system where the population of the two states is just given by $\hat{P}_3 = P \cdot \sigma_3$. Note that the 1, 2, 3 axes do not necessarily coincide with physical x, y, z directions but refer to the components of the Pauli matrices required to describe the two-level system in the Bloch sphere [10]. We can obtain the effective amplitude of the tunneling magnetoresistance as

$$a_{\text{TMR}}^* = a_{\text{TMR}} \cdot \frac{\langle \hat{P}_3 \rangle_{\text{th}}}{\sqrt{J(J+1)}} \cdot \cos(\alpha),$$

TABLE VI. Abundancies and relative confidence intervals obtained from the fit of Er and Tm XAS/XMCD spectra in Fig. 10 with the spectra simulated with atomic multiplet calculations including dimers. For the dimers, we indicate the abundance of the atoms in the form of dimers.

Er fit		Tm fit	
$4f^{11}$ O	67 ⁸⁸ / ₄₆ %	$4f^{13}$ O	77 ⁷⁸ / ₇₆ %
$4f^{11}$ bridge	11 ³² / ₀ %	$4f^{12}$ bridge	9 ¹⁰ / ₈ %
$4f^{11}$ dimers	22 ²³ / ₂₁ %	$4f^{12}$ dimers	14 ¹⁵ / ₁₃ %

where $\cos(\alpha)$ takes into account the projection of the atom's \mathbf{J} onto the tip polarization, and a_{TMR} is the maximal amplitude of the tunneling magnetoresistance realized with a complete flip of the total angular momentum. In lanthanide atoms, most of the tunneling magnetoresistance originates from the outer valence shells whose spins are coupled to the magnetic state of the $4f$ electrons. For atoms with a $\langle \vec{J} \rangle$ with a magnitude smaller than the total angular momentum \mathbf{J} , it is reasonable to rescale a_{TMR} by the factor $\frac{\langle \hat{P}_3 \rangle_{\text{th}}}{\sqrt{J(J+1)}}$, which considers the thermal equilibrium of the polarization $\langle \hat{P}_3 \rangle_{\text{th}}$ over its upper theoretical limit $\sqrt{J(J+1)}$. Note that $\langle \hat{P}_3 \rangle_{\text{th}}$ depends on $P = |\langle \vec{J} \rangle|$, on temperature, and on the energy level splitting. As such, it has a dependence on the external magnetic field intensity and angle.

For the sake of evaluating the model under the simplest experimental conditions, we consider an isotropic paramagnetic tip whose magnetization perfectly follows the direction of B_{ext} , i.e., $\alpha = \delta$ (Fig. 11). Although this assumption does not allow an accurate description of the angular dependence of the intensity in the case of tips showing bistability or magnetic anisotropy [10,56], the outcome of our model still provides a reasonable estimate for the maximum signal intensity. For the estimate of a_{TMR}^* , we consider a change in conductance a_{TMR}

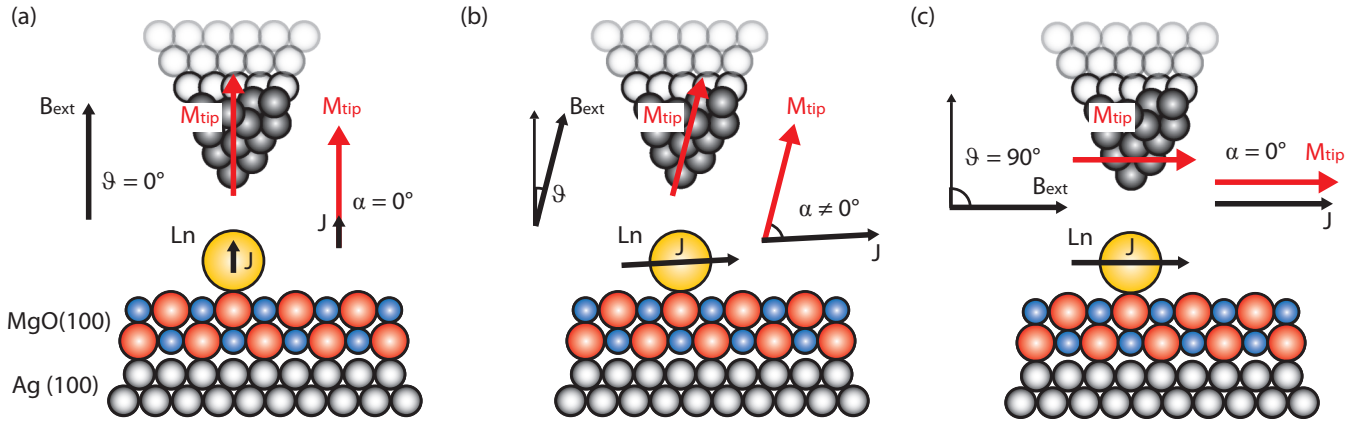


FIG. 11. Schematic of an ESR-STM experiment on a lanthanide atom ($\text{Ln} = \text{Er}, \text{Tm}$) based on the model used in the main text. The magnetic tip magnetization (M_{tip}) follows \mathbf{B}_{ext} while the high magnetic anisotropy of the lanthanide atom on the O adsorption site of MgO(100)/Ag(100) aligns the atom \mathbf{J} in plane. In the general case (b) of an external magnetic field angle ϑ different from 0° (a) or 90° (c), an angle α is present between the tip and the atom \mathbf{J} .

of around 4% as found in the contrast of spin-polarized STM experiments on Ho and Dy atoms on MgO(100)/Ag(100) [24,31,60], and we calculate $\langle \hat{P}_3 \rangle_{\text{th}}$ assuming a temperature of 1 K, typical for most ESR-STM systems.

The last parameters necessary to estimate the ESR-STM signal are the relaxation and coherence times T_1 and T_2 . As also mentioned in the main text, in the experimental conditions where the T_1 and T_2 are limited by the tunneling current, we consider $T_{1,2} \approx e/(r_{1,2}I)$ [59], where r is the probability for an electron to cause a relaxation event, e is the electron charge, and I is the sum of the dc and rf current taken as 10 pA. We estimate the value of $r_{1,2}$ starting from those of TiH from a previous work ($r_1 = 0.032$, $r_2 = 1$) [10]. Since the $4f$ electrons in lanthanides are strongly localized, and since the tunneling electrons only interact with them indirectly, namely via the valence shells [30,61], the decoherence and relaxation induced by the tunneling current is by order of magnitude smaller for these systems compared to $3d$ atoms [44]. Hence, we rescale both r_1 and r_2 by a factor 1/10 to account for the reduced current-related relaxation and decoherence events in lanthanides. Under these assumptions, and considering the value for the experimental parameters discussed above and reported in Table VII, we obtain an estimate for the angular and magnetic field intensity dependence of $\Delta I/I_{\text{dc}}$ [see Figs. 12(a) and 12(b)]. The gray dashed lines mark the parameter space corresponding to a constant $\Delta E/h$ frequency of 20 GHz that is used to represent the ESR signal in the plots shown in Figs. 12(c) and 12(d). We choose this representation to describe the typical experimental situation in which a limited frequency interval in the range of tens of GHz is available for transmitting rf power to the tunneling junction.

TABLE VII. Summary of the value for the experimental parameters used to estimate the model results for Er and Tm.

Parameter	a_{TMR}	T	Δz_{orf}	$\frac{dB_{\text{eff}}}{ds}$	r_1	r_2	I
Value	4%	1 K	0.4 pm	2 T/nm	0.0032	0.1	10 pA

The final estimation of the $\frac{\Delta I}{I_{\text{dc}}}$ predicts a maximum signal of around 0.9% for both Er and Tm. This value is smaller than what is typically measured in TiH and Fe, yet large enough to be detected in an ESR-STM experiment [6,10,55,56]. The maximum of the signal is reached for $\vartheta > 60^\circ$, corresponding to the angle at which the projection of \mathbf{J} onto the tip

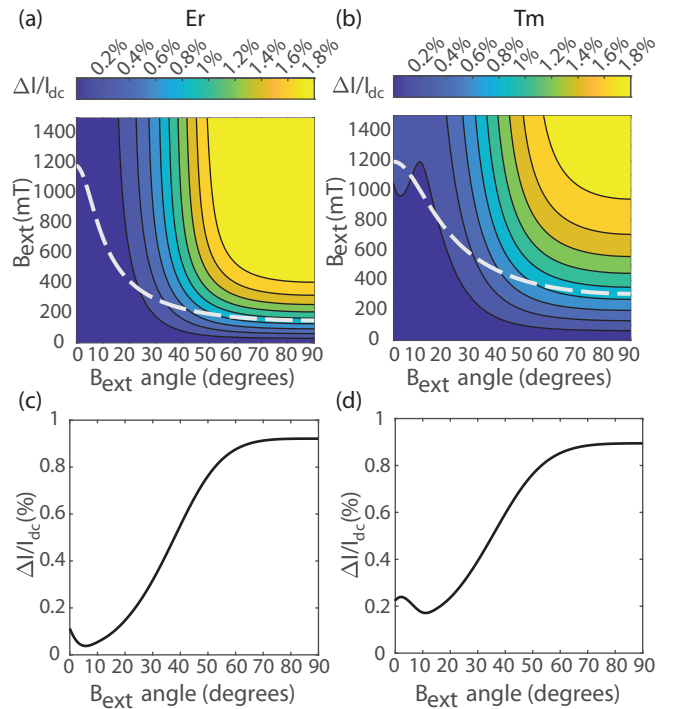


FIG. 12. Calculated ESR-STM signal for Er (a) and Tm (b). In the top panel, the signal is reported as a function of the external magnetic field intensity and angle. The dashed gray line represents the region with constant Zeeman splitting of 20 GHz. In the bottom panel, the signal at constant Zeeman splitting of 20 GHz is reported as a function of the external magnetic field angle for Er (c) and Tm (d).

polarization axis approaches the largest values. Even though at this angle the Rabi rate is close to its minimum, its value is still more than four times larger than that of TiH [6,10]. The nonmonotonic behavior at small angles is due to the rapid

change of alignment of \mathbf{J} with the tip polarization axis. The smallest values of α_{TMR}^* and signal intensity occur at around 5° (10°) for Er (Tm) for which the angle between \mathbf{J} and the tip polarization is maximum; see Fig. 11.

-
- [1] A. J. Heinrich, W. D. Oliver, L. M. K. Vandersypen, A. Ardavan, R. Sessoli, D. Loss, A. B. Jayich, J. Fernandez-Rossier, A. Laucht, and A. Morello, *Nat. Nanotechnol.* **16**, 1318 (2021).
- [2] D. M. Eigler and E. K. Schweizer, *Nature (London)* **344**, 524 (1990).
- [3] H. Brune, *Surf. Sci. Rep.* **31**, 125 (1998).
- [4] H. Brune, M. Giovannini, K. Bromann, and K. Kern, *Nature (London)* **394**, 451 (1998).
- [5] R. Baltic, M. Pivetta, F. Donati, C. Wackerlin, A. Singha, J. Dreiser, S. Rusponi, and H. Brune, *Nano Lett.* **16**, 7610 (2016).
- [6] S. Baumann, W. Paul, T. Choi, C. P. Lutz, A. Ardavan, and A. J. Heinrich, *Science* **350**, 417 (2015).
- [7] T. Choi, W. Paul, S. Rolf-Pissarczyk, A. J. Macdonald, F. D. Natterer, K. Yang, P. Willke, C. P. Lutz, and A. J. Heinrich, *Nat. Nanotechnol.* **12**, 420 (2017).
- [8] F. D. Natterer, F. Patthey, T. Bilgeri, P. R. Forrester, N. Weiss, and H. Brune, *Rev. Sci. Instrum.* **90**, 013706 (2019).
- [9] K. Yang, W. Paul, S. H. Phark, P. Willke, Y. Bae, T. Choi, T. Esat, A. Ardavan, A. J. Heinrich, and C. P. Lutz, *Science* **366**, 509 (2019).
- [10] T. S. Seifert, S. Kovarik, D. M. Juraschek, N. A. Spaldin, P. Gambardella, and S. Stepanow, *Sci. Adv.* **6**, eabc5511 (2020).
- [11] Y. Chen, Y. Bae, and A. J. Heinrich, *Adv. Mater.* 2107534 (2022).
- [12] X. Zhang, C. Wolf, Y. Wang, H. Aubin, T. Bilgeri, P. Willke, A. J. Heinrich, and T. Choi, *Nat. Chem.* **14**, 59 (2022).
- [13] R. Mirzoyan, N. P. Kazmierczak, and R. G. Hadt, *Chem. Eur. J.* **27**, 9482 (2021).
- [14] A. Abragam and B. Bleaney, *Electron Paramagnetic Resonance of Transition Ions* (Clarendon, Oxford, 1970).
- [15] E. D. Herbschleb, H. Kato, Y. Maruyama, T. Danjo, T. Makino, S. Yamasaki, I. Ohki, K. Hayashi, H. Morishita, M. Fujiwara, and N. Mizuochi, *Nat. Commun.* **10**, 3766 (2019).
- [16] I. G. Rau, S. Baumann, S. Rusponi, F. Donati, S. Stepanow, L. Gragnaniello, J. Dreiser, C. Piamonteze, F. Nolting, S. Gangopadhyay, O. R. Albertini, R. M. Macfarlane, C. P. Lutz, B. A. Jones, P. Gambardella, A. J. Heinrich, and H. Brune, *Science* **344**, 988 (2014).
- [17] K. Yang, Y. Bae, W. Paul, F. D. Natterer, P. Willke, J. L. Lado, A. Ferr3n, T. Choi, J. Fernandez-Rossier, A. J. Heinrich, and C. P. Lutz, *Phys. Rev. Lett.* **119**, 227206 (2017).
- [18] K. Yang, P. Willke, Y. Bae, A. Ferr3n, J. L. Lado, A. Ardavan, J. Fernandez-Rossier, A. J. Heinrich, and C. P. Lutz, *Nat. Nanotechnol.* **13**, 1120 (2018).
- [19] S. Kovarik, R. Robles, R. Schlitz, T. S. Seifert, N. Lorente, P. Gambardella, and S. Stepanow, *Nano Lett.* **22**, 4176 (2022).
- [20] P. Willke, T. Bilgeri, X. Zhang, Y. Wang, C. Wolf, H. Aubin, A. Heinrich, and T. Choi, *ACS Nano* **15**, 17959 (2021).
- [21] D. P. DiVincenzo, *Fortschr. Phys.* **48**, 771 (2000).
- [22] F.-S. Guo, B. M. Day, Y.-C. Chen, M.-L. Tong, A. Mansikkamaki, and R. A. Layfield, *Science* **362**, 1400 (2018).
- [23] F. Donati, S. Rusponi, S. Stepanow, C. Wackerlin, A. Singha, L. Persichetti, R. Baltic, K. Diller, F. Patthey, E. Fernandes, J. Dreiser, Z. Slijivancanin, K. Kummer, C. Nistor, P. Gambardella, and H. Brune, *Science* **352**, 318 (2016).
- [24] A. Singha, P. Willke, T. Bilgeri, X. Zhang, H. Brune, F. Donati, A. J. Heinrich, and T. Choi, *Nat. Commun.* **12**, 4179 (2021).
- [25] M. Shiddiq, D. Komijani, Y. Duan, A. Gaita-Arino, E. Coronado, and S. Hill, *Nature (London)* **531**, 348 (2016).
- [26] J. V. Rakonjac, Y.-H. Chen, S. P. Horvath, and J. J. Longdell, *Phys. Rev. B* **101**, 184430 (2020).
- [27] K. S. Pedersen, A.-M. Ariciu, S. McAdams, H. Weihe, J. Bendix, F. Tuna, and S. Piligkos, *J. Am. Chem. Soc.* **138**, 5801 (2016).
- [28] N. Kukharchyk, D. Sholokhov, O. Morozov, S. L. Korableva, A. A. Kalachev, and P. A. Bushev, *New J. Phys.* **20**, 023044 (2018).
- [29] M. Rancic, M. P. Hedges, R. L. Ahlefeldt, and M. J. Sellars, *Nat. Phys.* **14**, 50 (2018).
- [30] M. Pivetta, F. Patthey, I. Di Marco, A. Subramonian, O. Eriksson, S. Rusponi, and H. Brune, *Phys. Rev. X* **10**, 031054 (2020).
- [31] F. D. Natterer, K. Yang, W. Paul, P. Willke, T. Y. Choi, T. Greber, A. J. Heinrich, and C. P. Lutz, *Nature (London)* **543**, 226 (2017).
- [32] C. Bonizzoni, A. Ghirri, K. Bader, J. van Slageren, M. Perfetti, L. Sorace, Y. Lan, O. Fuhr, M. Ruben, and M. Affronte, *Dalton Trans.* **45**, 16596 (2016).
- [33] A. Singha, F. Donati, C. Wackerlin, R. Baltic, J. Dreiser, M. Pivetta, S. Rusponi, and H. Brune, *Nano Lett.* **16**, 3475 (2016).
- [34] F. Donati, A. Singha, S. Stepanow, C. Wackerlin, J. Dreiser, P. Gambardella, S. Rusponi, and H. Brune, *Phys. Rev. Lett.* **113**, 237201 (2014).
- [35] A. Singha, R. Baltic, F. Donati, C. Wackerlin, J. Dreiser, L. Persichetti, S. Stepanow, P. Gambardella, S. Rusponi, and H. Brune, *Phys. Rev. B* **96**, 224418 (2017).
- [36] J. D. Rinehart and J. R. Long, *Chem. Sci.* **2**, 2078 (2011).
- [37] F. Donati, S. Rusponi, S. Stepanow, L. Persichetti, A. Singha, D. M. Juraschek, C. Wackerlin, R. Baltic, M. Pivetta, K. Diller, C. Nistor, J. Dreiser, K. Kummer, E. Velez-Fort, N. A. Spaldin, H. Brune, and P. Gambardella, *Phys. Rev. Lett.* **124**, 077204 (2020).
- [38] A. Singha, D. Sostina, C. Wolf, S. L. Ahmed, D. Krylov, L. Colazzo, P. Gargiani, S. Agrestini, W. S. Noh, J. H. Park, M. Pivetta, S. Rusponi, H. Brune, A. J. Heinrich, A. Barla, and F. Donati, *ACS Nano* **15**, 16162 (2021).
- [39] L. Ungur and L. F. Chibotaru, *Inorg. Chem.* **55**, 10043 (2016).
- [40] J. Pal, M. Smerieri, E. Celasco, L. Savio, L. Vattuone, and M. Rocca, *Phys. Rev. Lett.* **112**, 126102 (2014).
- [41] F. Donati, M. Pivetta, C. Wolf, A. Singha, C. Wackerlin, R. Baltic, E. Fernandes, J. G. de Groot, S. L. Ahmed, L. Persichetti, C. Nistor, J. Dreiser, A. Barla, P. Gambardella, H. Brune, and S. Rusponi, *Nano Lett.* **21**, 8266 (2021).

- [42] E. Fernandes, F. Donati, F. Patthey, S. Stavrić, Ž. Šljivančanin, and H. Brune, *Phys. Rev. B* **96**, 045419 (2017).
- [43] E. Fernandes, Ph.D. thesis No. 8144, EPFL, Lausanne, 2017.
- [44] W. Paul, K. Yang, S. Baumann, N. Romming, T. Choi, C. P. Lutz, and A. J. Heinrich, *Nat. Phys.* **13**, 403 (2017).
- [45] C. Piamonteze, U. Flechsig, S. Rusponi, J. Dreiser, J. Heidler, M. Schmidt, R. Wetter, M. Calvi, T. Schmidt, H. Pruchova, J. Krempasky, C. Quitmann, H. Brune, and F. Nolting, *J. Synch. Radiat.* **19**, 661 (2012).
- [46] M. W. Haverkort, *J. Phys. Conf. Ser.* **712**, 012001 (2016).
- [47] R. D. Cowan, *The Theory of Atomic Structure and Spectra* (University of California Press, Berkeley, CA, 2012).
- [48] P. Giannozzi, S. Baroni, N. Bonini, M. Calandra, R. Car, C. Cavazzoni, D. Ceresoli, G. L. Chiarotti, M. Cococcioni, I. Dabo, A. Dal Corso, S. de Gironcoli, S. Fabris, G. Fratesi, R. Gebauer, U. Gerstmann, C. Gougoussis, A. Kokalj, M. Lazzeri, L. Martin-Samos, N. Marzari, F. Mauri, R. Mazzarello, S. Paolini, A. Pasquarello, L. Paulatto, C. Sbraccia, S. Scandolo, G. Sclauzero, A. P. Seitsonen, A. Smogunov, P. Umari, and R. M. Wentzcovitch, *J. Phys. Condens. Matter* **21**, 395502 (2009).
- [49] G. Prandini, A. Marrazzo, I. E. Castelli, N. Mounet, and N. Marzari, *npj Comput. Mater.* **4**, 72 (2018).
- [50] F. Donati and A. J. Heinrich, *Appl. Phys. Lett.* **119**, 160503 (2021).
- [51] C. Nistor, A. Mugarza, S. Stepanow, P. Gambardella, K. Kummer, J. L. Diez-Ferrer, D. Coffey, C. de la Fuente, M. Ciria, and J. I. Arnaudas, *Phys. Rev. B* **90**, 064423 (2014).
- [52] R. Baltic, F. Donati, A. Singha, C. Wäckerlin, J. Dreiser, B. Delley, M. Pivetta, S. Rusponi, and H. Brune, *Phys. Rev. B* **98**, 024412 (2018).
- [53] M. Pivetta, S. Rusponi, and H. Brune, *Phys. Rev. B* **98**, 115417 (2018).
- [54] A. G. Fowler, *Phys. Rev. A* **88**, 042308 (2013).
- [55] Y. Bae, K. Yang, P. Willke, T. Choi, A. J. Heinrich, and C. P. Lutz, *Sci. Adv.* **4**, eaau4159 (2018).
- [56] J. Kim, W.-j. Jang, T. H. Bui, D.-J. Choi, C. Wolf, F. Delgado, Y. Chen, D. Krylov, S. Lee, S. Yoon, C. P. Lutz, A. J. Heinrich, and Y. Bae, *Phys. Rev. B* **104**, 174408 (2021).
- [57] F. Delgado and N. Lorente, *Prog. Surf. Sci.* **96**, 100625 (2021).
- [58] J. L. Lado, A. Ferrón, and J. Fernández-Rossier, *Phys. Rev. B* **96**, 205420 (2017).
- [59] P. Willke, W. Paul, F. D. Natterer, K. Yang, Y. Bae, T. Choi, J. Fernández-Rossier, A. J. Heinrich, and C. P. Lutz, *Sci. Adv.* **4**, eaaq1543 (2018).
- [60] F. D. Natterer, F. Donati, F. Patthey, and H. Brune, *Phys. Rev. Lett.* **121**, 027201 (2018).
- [61] D. Coffey, J. L. Diez-Ferrer, D. Serrate, M. Ciria, C. d. l. Fuente, and J. I. Arnaudas, *Sci. Rep.* **5**, 13709 (2015).